Nanoscale n++-p junction formation in GeOI probed by tip-enhanced Raman spectroscopy and conductive atomic force microscopy

Prucnal, S.; Berencen, Y.; Wang, M.; Georgiev, Y.; Erbe, A.; Khan, M. B.; Böttger, R.; Hübner, R.; Schönherr, T.; Kalbacova, J.; Vines, L.; Facsko, S.; Engler, M.; Zahn, D. R. T.; Knoch, J.; Helm, M.; Skorupa, W.; Zhou, S.;

Originally published:

June 2019

Journal of Applied Physics 125(2019), 245703

DOI: https://doi.org/10.1063/1.5080289

Perma-Link to Publication Repository of HZDR:

https://www.hzdr.de/publications/Publ-29401

Nanoscale n^{++}-p junction formation in GeOI probed by tip-enhanced Raman spectroscopy and conductive atomic force microscopy

Slawomir Prucnal[1,*], Yonder Berencén[1], Mao Wang[1], Yordan M. Georgiev[1,§], Artur Erbe[1], Muhammad B. Khan[1], Roman Boettger[1], René Hübner[1], Tommy Schönherr[1], Jana Kalbacova[4], Lasse Vines[6], Stefan Facsko[1], Martin Engler[1], Dietrich R. T. Zahn[2], Joachim Knoch[3], Manfred Helm[1,5], Wolfgang Skorupa[1] and Shengqiang Zhou[1]

[1]Helmholtz-Zentrum Dresden-Rossendorf, Institute of Ion Beam Physics and Materials Research, Bautzner Landstraße 400, D-01328 Dresden, Germany

[2]Semiconductor Physics, Technische Universität Chemnitz, Reichenhainer Straße 70, D-09107 Chemnitz, Germany

[3]Institut für Halbleitertechnik, RWTH Aachen, Germany

[4]HORIBA Jobin Yvon GmbH, Neuhofstr. 9, D-64625 Bensheim, Germany

[5]Center for Advancing Electronics Dresden (cfaed), Technische Universität Dresden, 01062 Dresden, Germany

[6]Department of Physics/Centre for Materials Science and Nanotechnology, University of Oslo, P.O. Box 1048 Blindern, N-0316 Oslo, Norway

* To whom correspondence should be addressed: s.prucnal@hzdr.de

§ On leave of absence from the Institute of Electronics at the Bulgarian Academy of Sciences, Sofia, Bulgaria

Abstract

Ge-on-Si and Ge-on-insulator (GeOI) are the most promising materials for the next-generation nanoelectronics that can be fully integrated with silicon technology. To this day, the fabrication of Ge-based transistors with a n-type channel doping above 5×10^{19} cm^{-3} remains challenging. Here we report on n-type doping of Ge beyond the equilibrium solubility limit ($n_e \approx 6\times10^{20}$ cm^{-3}) together with a nanoscale technique to inspect the dopant distribution in n^{++}-p junctions in GeOI. The n^{++} layer in Ge is realized by P^+ ion implantation followed by millisecond-flash lamp annealing. The electron concentration is found to be three times higher than the equilibrium solid solubility limit of P in Ge determined at 800 ºC. The millisecond-flash lamp annealing process is used for the electrical activation of the implanted P dopant and to fully suppress its diffusion. The study of the P activation and distribution in implanted GeOI relies on the combination of Raman spectroscopy, conductive atomic force microscopy and secondary ion mass spectrometry. The linear dependence between the Fano asymmetry parameter q and the active carrier concentration makes Raman spectroscopy a powerful tool to study the electrical properties of semiconductors. We also demonstrate the high electrical activation efficiency together with the formation of ohmic contacts through Ni germanidation via a single-step flash lamp annealing process.

Keywords: germanium, c-AFM, TERS, n-type doping, GeOI, ion implantation, flash lamp annealing

1. Introduction

The first transistor was made of Ge in 1948. However, Ge was fully replaced by Si in microelectronics, because of technological hurdles: the lack of a stable oxide, doping issues and problems with the formation of low-resistance ohmic contacts with n-type Ge. Nowadays, the Si-based complementary metal-oxide-semiconductor (CMOS) technology is at its limit. Further miniaturization of electronic devices would require new solutions for patterning and doping of channel materials [1]. Therefore, the integration of high carrier mobility semiconductors with CMOS technology is very promising. Initially, III-V compound semiconductors were considered for integration with Si, but the III-V approach has fundamental physical limitations, like unstable gate dielectric, high source to drain leakage, low hole mobility in most of the III-V semiconductors, etc. This alternative is also expensive and difficult to integrate with the existing technology [2, 3]. Ge, however, is one of the most promising candidates that can complement or even replace Si in future nanoelectronics [4-6]. In general, Ge is the most Si-compatible high-mobility channel material. The electron and hole mobilities in Ge are about two and four times higher than that of Si, respectively. Moreover, the carrier mobility in Ge can be easily enhanced by alloying Ge with Sn and strain engineering [7-10]. The Si chemistry and high-k gate oxides can also be adopted for Ge which makes the integration of Ge with Si even more attractive. The remaining challenges in Ge nanoelectronics are ultra-high n-type doping and a low specific contact resistance (ρ_c) in n-type Ge. Recently, different approaches have been developed to realize ultra-high n-type doping in Ge *e.g.* multi-step ion implantation [11], molecular beam epitaxy (MBE) delta doping [12], ion implantation followed by pulsed laser annealing [13] or flash lamp annealing [14,15], and molecular doping [16].

In addition, different techniques have also been reported to probe and visualize the dopant

distribution in semiconductors after the doping procedure. In recent years, scanning spreading resistance microscopy (SSRM) has become one of the main methods of choice for two-dimensional carrier profiling in Si- and Ge-based nanostructures [17-19]. Carrier profiling in thin semiconductor films can also be obtained using electrochemical capacitance-voltage (ECV) profiling. ECV is commonly used to determine the doping level in group IV semiconductors (Si, Ge, SiGe) as well as in III-V compound semiconductors [20]. In contrast to secondary ion mass spectrometry (SIMS), ECV provides a depth profile of electrically active dopants. Moreover, different dopants in Ge or Si can also be detected through Raman spectroscopy by measuring the local vibrational phonon mode and Fano effect [21-24]. Both the peak intensity of the Ge-P local vibrational phonon mode and the Fano parameter Γ are determined by the P concentration while the Fano asymmetry parameter q is proportional to the electrically active P dopants and the absolute value of q decreases with increasing the carrier concentration. Moreover, the peak position of Ge-P phonon mode shifts towards higher wavenumbers with increasing P concentration. Additionally, for the very high P concentration the Ge-P phonon mode can broaden due to the formation of electrically inactive P-P dimers. The low specific contact resistance on n-type Ge is mainly realized by germanidation of Ni during rapid thermal annealing (RTA) [25, 26]. To this day, stoichiometric NiGe on n-type Ge shows the best performance in terms of ohmic contacts.

In this paper, we present a novel methodology to explore the carrier distribution in ultra-doped germanium using Raman spectroscopy. The n^{++}-p junction in GeOI is realized by ion implantation of P into p-type Ge followed by rear-side flash lamp annealing (FLA) for 20 ms [14, 27]. The maximum electron concentration calculated from the Raman spectra and confirmed by Hall effect measurement is found to be in the order of 6×10^{20} cm^{-3} which is the highest value ever published for n-type Ge. The depth distribution of P in ion-implanted GeOI and the formation of n^{++}-p

junction in GeOI are probed by tip-enhanced Raman spectroscopy (TERS) and conductive atomic force microscopy (c-AFM), respectively. The TERS and the c-AFM signals are recorded along a bevel made in GeOI using e-beam lithography and reactive ion etching. c-AFM is also used to visualize the n-type, the p-type and the depleted regions in the n^{++}-p junction. During the same single flash pulse, a 10 nm thick Ni film, previously deposited on top of the P-doped Ge layer, diffuses into Ge forming a stoichiometric NiGe layer. We demonstrate that this single-step FLA processing of P-implanted Ge prevents the unwanted deactivation of carriers and P diffusion, which were reported to occur in Ge during conventional annealing [28].

2. Methods

2.1 Sample preparation

Ge-on-insulator (GeOI) samples with 200 nm thick highly p-type doped (1×10^{19} cm^{-3}) Ge layer (IQE Advanced Silicon) or intrinsic GeOI samples were implanted with P ions with different fluences ranging from 5×10^{14} cm^{-2} to 5×10^{15} cm^{-2} and at an energy of 20 keV corresponding to P concentrations of 1, 3, 5, 7, and 10×10^{20} cm^{-3}. The Si substrate and the oxide layer were 675 μm and 150 nm thick, respectively. The distribution of P in Ge was calculated using the stopping and range of ions in matter (SRIM) code [29] and confirmed by secondary ion mass spectrometry (SIMS). Prior to ion implantation, a 20 nm thick SiO_2 layer was deposited by plasma-enhanced chemical vapour deposition (PECVD). The oxide layer was used to protect the Ge surface during ion implantation and in turn to suppress the out-diffusion of P during post-implantation annealing. The post-implantation annealing was performed for 20 ms using FLA applied to the rear side of the sample [14]. The maximum surface temperature during FLA was estimated to be about 850 ºC and the energy density deposited onto the sample surface was in the range of 90 to 125 Jcm^{-2}. After

annealing, the SiO_2 layer was removed in a buffered hydrofluoric acid. To investigate the specific contact resistance of NiGe made by in-diffusion of Ni into P implanted Ge during millisecond range FLA, the following process flow was carried out: (1) the SiO_2 capping layer was removed from the as-implanted sample, (2) Ni stripes were deposited on the Ge (for the transfer length method, TLM), (3) deposition of a SiO_2 capping layer at RT by sputtering, (4) FLA and (5) etching of SiO_2 capping layer in HF. The formation of ohmic contacts to n-type Ge was realized by germanidation of a 10 nm thick Ni layer. The germanidation was done *in-situ* together with the P activation within a single flash pulse of 20 ms at an energy density of 95 Jcm^{-2}.

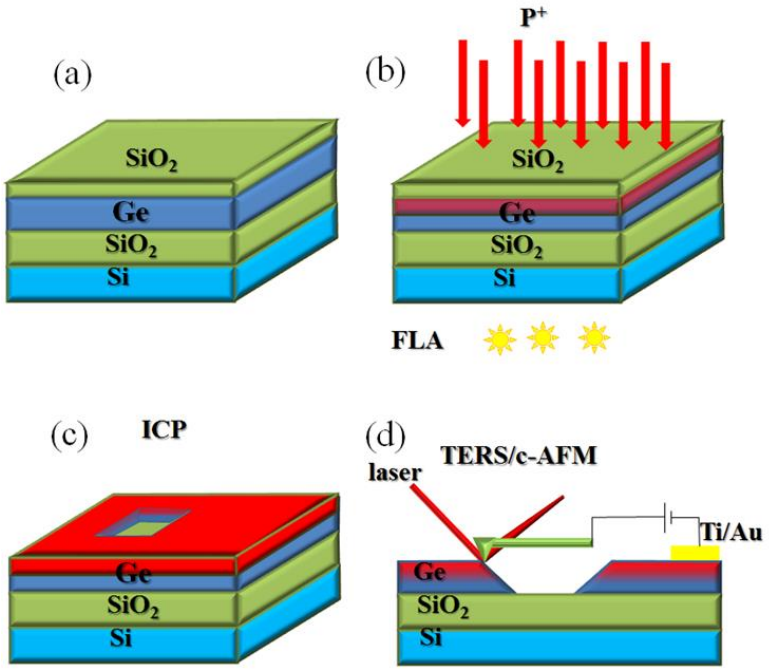

FIG. 1. Schematic representation of the fabrication and the characterization processes of a shallow n^{++}-p junction in GeOI: 200 nm thick p-type GeOI wafer covered with a 20 nm thick SiO_2 protective layer deposited by PECVD (a), ion implantation followed by rear-side FLA (b), bevel formation by e-beam lithography and inductively coupled plasma (ICP) etching (c), schematic cross-section of the bevel (d).

In order to obtain the in-depth distribution of electrically active P atoms, the peak intensity of the Ge-P phonon mode was monitored by tip-enhanced nano-Raman spectroscopy (TERS). Prior to this step, a lithographically defined 50×50 μm square was etched by inductively coupled plasma (ICP) using a SF_6 and C_4F_8 plasma (see Fig. 1c). The ICP etching parameters were optimized for the under-etching of Ge below the polymer mask (etching parameters: SF_6: 12 sccm, C_4F_8: 20 sccm, ICP power: 400 W, platen power: 12 W, pressure 1.13 Pa). These conditions resulted in the formation of a bevel schematically shown in Fig. 1 (d). The experimental process flow for samples intended for TERS/c-AFM characterization is as follows: 1) deposition of a capping layer (Fig. 1a), 2) ion implantation (Fig. 1b), 3) rear-side FLA, 4) removal of the capping layer, 5) e-beam lithography, 6) ICP (SF_6+C_4F_8) (Fig. 1c), 7) electrical contact formation, and 8) characterization by TERS and c-AFM (Fig. 1d). The electrical contacts for c-AFM were performed on the previously flash-lamp annealed samples. To this end, we have exclusively used Ti/Au contacts for c-AFM experiments that are sufficiently good to provide ohmic contact to highly doped n-type Ge.

2.2. Sample characterization

P concentration versus depth profiles were measured by SIMS employing a Cameca IMS7f micro-analyzer. A beam of 15 keV Cs^+ ions was rastered over a surface area of 200×200 μm^2 and secondary ions were collected from the central part of the sputtered crater. Crater depths were measured with a Dektak 8 stylus profilometer, and a constant erosion rate was assumed when converting the sputtering time to sample depth. Calibration of the P signal was performed using the as-implanted sample as a reference. The electrical properties of the implanted and the annealed GeOI samples were determined by Hall effect measurements using a commercial Lakeshore Hall System with van der Pauw configuration in the temperature range of 2 to 300 K. Figure 2 shows

the electron concentration as a function of P concentration obtained from implanted and annealed samples at 2.5 K and 300K, respectively. The thickness of the doped layers (P distribution) used to calculate the active carrier concentration was taken from SIMS measurements. For the lowest P concentration (1×10^{20} cm^{-3}), the activation efficiency of P implanted into Ge is above 80 % and slightly decreases with increasing P concentration. Finally, for the P concentration as high as 1×10^{21} cm^{-3} the activation efficiency is in the range of 60 %.

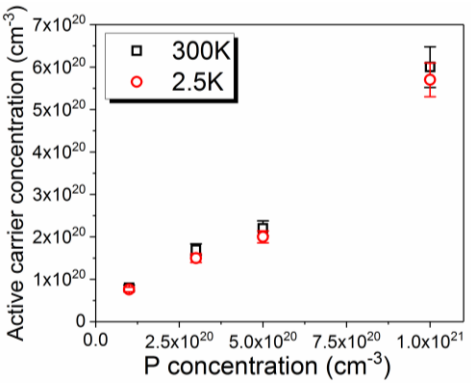

Figure 2. Active carrier concentration as a function of P concentration estimated from Hall effect measurements at 2.5 (red circles) and 300 K (black squares).

The electron concentration obtained at RT is a slightly lower. Some of defects in Ge are acceptors, which donate holes into the matrix. Śpiewak *et al.* using density functional theory with local density approximation including on-site Coulomb interaction have shown that vacancies in Ge have two acceptor levels for different ionization states (0/1-) and (1-/2-) [30]. The first acceptor level for (0/1-) is located about 0.02 eV and the second level for (1-/2-) is located about 0.26 eV above the valence band maximum. Taking into account the very high electron concentration in the investigated samples, we assume that most of vacancies are in their highest charging state. Therefore, they are deep acceptors and cannot provide holes into the matrix at low temperature. Hence, the measured effective carrier concentration at 2.5 K corresponds to the concentration of electrically active P atoms in the substitutional position.

The Raman active phonon modes were investigated by micro-Raman and TERS using green (532 nm) and red (632 nm) lasers for excitation, respectively. TERS experiments were performed in side-illumination/side-collection configuration (XploRa NanoRaman^{TM} platform, HORIBA Scientific). The achieved lateral resolution for TERS is in the range of 8 nm as determined on a reference sample with a silver coated TERS tip (Omni^{TM} TERS probes, HORIBA Scientific) [31]. The n^{++}-p junction was visualized by c-AFM (Bruker MM8) using a diamond coated conductive n^{+}-silicon tip (CDT-CONTR-10), with a resistivity of 0.01 – 0.02 Ωcm and a logarithmic current amplifier. Prior to c-AFM measurements, samples were cleaned in deionized water for native oxide (GeO_x) removal. The obtained c-AFM images were analyzed by the software Gwyddion. The measurements of contact resistance on the formed NiGe contacts were carried out using the TLM. 200 μm long × 50 μm wide Ni stripes separated by 10, 20, 40, 60, 80 and 100 μm were deposited on Ge using optical lithography and the lift-off method. The TLM structures allow to extract the contact resistance (R_c), the transfer length (L_T), and the sheet resistance (R_s) from which the specific contact resistance (ρ_c) is subsequently calculated. To investigate the microstructural properties of the Ni-germanide layer, cross-sectional transmission electron microscopy (TEM) investigations were performed on a Titan 80-300 (FEI) microscope operated at an accelerating voltage of 300 kV. High-angle annular dark-field scanning transmission electron microscopy (HAADF-STEM) imaging and element mapping based on energy-dispersive X-ray spectroscopy (EDXS) were performed at 200 kV with a Talos F200X microscope equipped with a Super-X EDXS detector system (FEI). Prior to TEM analysis, the specimen mounted in a high-visibility low-background holder was placed for 10 s into a Model 1020 Plasma Cleaner (Fischione) to remove organic contamination.

3. Results and discussion

Figure 3a shows the 3D topographic mapping of the bevel formed in GeOI using e-beam lithography and ICP etching obtained by c-AFM measurements and the cross-section schematic representation of the fabricated n^{++}-p junction. The P concentration in the n^{++}-layer is 1×10^{21} cm^{-3} and the sample was annealed for 20 ms at an energy density of 95 Jcm^{-2}. Fig. 3b shows the 2D c-AFM image obtained from the bevel made in the P-implanted and annealed GeOI sample. The colour code, from brown/red to blue/white, correspond to low and high resistive regions, respectively.

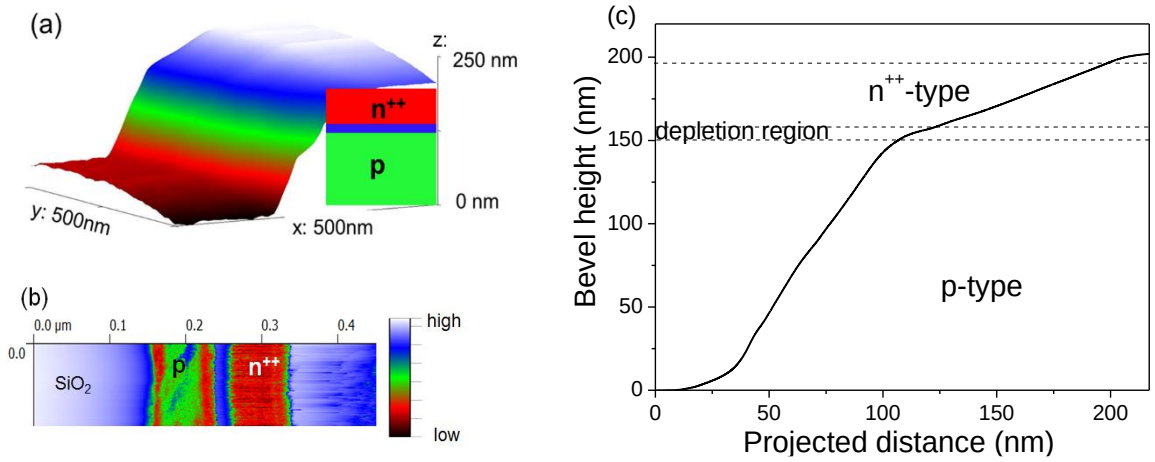

FIG. 3. The topography of the bevel (a) and the resistance mapping over the n^{++}-p junction (b). The blue and red colours correspond to high and low resistive regions, respectively. (c) shows the bevel height projected on the xz plane obtained by c-AFM measurement. The P implanted GeOI was annealed for 20 ms at an energy density of 95 Jcm^{-2}.

According to c-AFM measurements (Fig. 3b), three regions within the bevel can readily be distinguished: (i) a highly conductive n^{++} top layer due to the P doping, (ii) a depletion region at the interface between n^{++}- and p-type Ge and (iii) the p-type Ge. The highly resistive left and right parts (blue) of the c-AFM image corresponds to the SiO_2 (buried oxide) layer in GeOI and residual

capping oxide, respectively. In general, the profile of the etched bevels depends on the etching parameters, such as plasma composition, temperature, power and pressure [32]. Either reactive ion etching (RIE) or ICP etching of Si and Ge are usually carried out with halogen-based chemistries (Cl_2, CF_4, SF_6 and HBr). The ICP etching of Si and Ge is isotropic. Castro *et al.* have shown that using Cl_2/N_2 plasma, it is possible to etch Ge selectively from the Si substrate with an anisotropic etching profile [32]. The etching selectivity of Ge and Si is 116 i.e. the etching rate of Ge compared to the etching rate of Si using Cl_2/N_2 plasma is 116 times faster. Using different plasma parameters, the etching profile of intrinsic Ge can be precisely controlled. This is, however, more challenging in doped materials. Lee and Chen have investigated the influence of the doping level in Si on the etching rate during halogen-based RIE [33]. It was found that for doping levels below 10^{18} cm^{-3} the etching rate is roughly the same in p- and n-type Si. On the contrary, it changes significantly for doping levels above 10^{19} cm^{-3}. For example, in P or As (n-type) heavily doped Si, the Coulomb attraction between uncompensated donors and chemisorbed halogens increases the etching rate of Si, whereas in case of p-type Si the Coulomb repulsion between uncompensated acceptors and chemisorbed halogens decreases the etching rate [33]. Because of the similarity between Si and Ge the same mechanism is expected to take place in Ge during RIE. In fact, the different slopes of the bevel profile presented in Fig. 3c clearly evidence the variation of the etching rate as a function of Ge doping. From the shape of the etching profile, the thickness of individual layers can be determined (n^{++} layer, depletion layer and p-type layer). The n^{++} layer is etched with the highest etching rate and reveals a thickness of about 40 nm. Likewise, the depletion and the residual p-type layers are about 8 and 152 nm thick, respectively. The thickness of the n^{++} layer estimated from c-AFM measurements fits well with the P distribution in Ge predicted by the SRIM code and measured by SIMS. Figure 4a shows the depth distribution of P in the as-implanted (black squares)

and annealed (red circles) samples. The FLA was performed for 20 ms at an energy density of 95 Jcm^{-2} in N_2 ambient. P was implanted through the SiO_2 layer and the projected ion range (R_p) was designed to be slightly below the SiO_2/Ge interface, R_p~30 nm. Therefore, after removing the capping layer, the maximum concentration of P is close to the Ge surface. The P concentration monotonically decreases below 20 nm which is expected for the ion implanted layer with Gaussian distribution of implanted dopants. At the depth of about 50 nm, the P concentration is equal to the B concentration in the virgin sample (in the range of 1×10^{19} cm^{-3}). After annealing and activation of the implanted P ions, the n^{++} layer results in a thickness of about 40 nm. This is in good agreement with the data obtained by c-AFM where the highly resistive layer (depletion region) is detected to be about 40 nm from the Ge surface.

The increase of the ^{31}P signal below 180 nm in SIMS profile is due to an interference of ^{31}P signal with ^{30}Si from the oxide layer beneath Ge and H, which is always present in the system (the mass of ^{31}P is almost the same as the mass of ^{30}Si + H). Recently, we have shown that after ion implantation and rear-side FLA, the P distribution in Ge is not affected by the annealing [14]. The same behaviour is observed in the GeOI sample. This means that the millisecond range rear-side FLA process fully suppresses the diffusion of P atoms in Ge, even in the case when the P concentration is much higher than the equilibrium solid solubility at 800 ºC. Due to high fluence P implantation it is expected that the n^{++} layer might be contaminated with oxygen which can be introduced into Ge *via* recoil implantation from the capping layer. In the present work, a SiO_2 capping layer grown by PECVD has been used. Unfortunately, oxygen has negative influence on the electrical properties of Ge [34]. Therefore, the SiO_2 layer is not the best choice to protect the Ge surface from sputtering/roughening during ion implantation. In the future, different capping layers will be tested, *e.g.* amorphous Si or Si_3N_4.

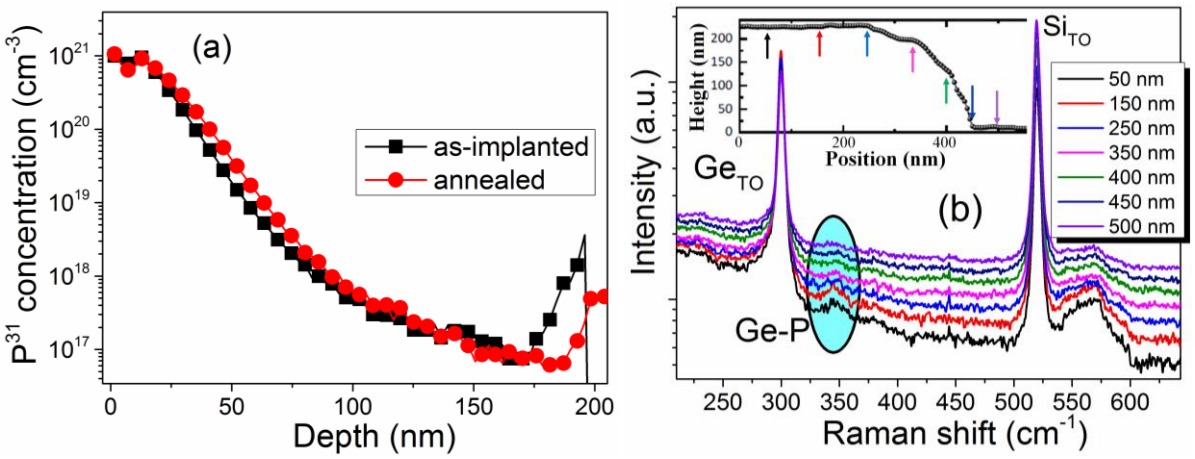

FIG. 4. The depth distribution of P in Ge obtained for the as-implanted and annealed samples using SIMS (a) and phonon spectra obtained from heavily doped n-type Ge using TERS at different lateral bevel positions (b). The inset in (b) shows the bevel shape and the measurement points along the bevel which are marked with different colour arrows. Prior to the measurements, the SiO_2 layer was removed by etching in HF. GeOI samples used for SIMS and TERS were implanted with P at a fluence of 5×10^{15} cm^{-2} (P concentration ~ 1×10^{21} cm^{-3}) and flash-lamp annealed for 20 ms at an energy density of 95 Jcm^{-2}.

Figure 4b shows tip-enhanced Raman spectra under 632 nm laser excitation obtained from P-implanted and annealed GeOI at different positions starting from the unmodified area (curves 50 and 150 nm), through the bevel (curves 250, 350 and 400 nm) to the bottom of the etched area (curves 450 and 500 nm). The two main phonon modes are located at 300.5 cm^{-1} and 520 cm^{-1} which are ascribed to the longitudinal/transverse optical (LO/TO) phonon modes in Ge (TO_{Ge-Ge}) and Si (TO_{Si-Si}), respectively. The TO_{Si-Si} phonon mode is observed from the GeOI substrate. The broad band spanning from 530 to 600 cm^{-1} comes from the second order Raman scattering in Ge. The TO_{Ge-Ge} phonon mode at 300.5 cm^{-1} can be asymmetric due to the Fano effect commonly

observed in highly-doped group-IV semiconductors [35-37]. The broadening of the Raman spectrum towards lower wavenumbers is observed both in n-type and p-type doped Ge and it is attributed to the Fano interference caused by coupling between discrete optical phonons and carriers [36]. Moreover, the TERS spectra exhibit a well distinguishable peak at about 342 cm^{-1}. This phonon mode is related to the local vibration mode between P and Ge atoms [21]. The peak position of Ge-P local vibrational phonon mode is defined by the structure quality and the concentration of P atoms. With decreasing P concentration, the Ge-P phonon mode shifts towards lower wavenumbers [21]. In fact, moving the tip towards the bottom part of the bevel causes i) a shift of the Ge-P phonon mode from 346.5±1 cm^{-1} (curves 50 and 150 nm) to 344±1 cm^{-1} (curve 350 nm) and ii) a decrease of its overall intensity. This is due to the decrease of the P concentration within the depth, which is in good agreement with the results obtained by c-AFM and SIMS. The Fano effect in heavily doped Ge and the influence of the P concentration on the peak position and intensity of the Ge-P local vibrational phonon mode was further investigated by a conventional micro-Raman setup using 532 nm laser light for excitation and samples with well-defined P concentration (see Fig. 5). The P concentration in the Ge layer varies from 1×10^{20} to 1×10^{21} cm^{-3}. After FLA, n^+ layers with an effective carrier concentration up to 6×10^{20} cm^{-3} are achieved. Figure 5a shows the $TO_{Ge\text{-}Ge}$ phonon mode in normalized Raman spectra of heavily P doped Ge. The peak shift towards shorter wavenumbers and the asymmetric broadening of the peak are due to the increasing of effective carrier concentration with increasing the doping concentration. The local vibrational phonon mode of Ge-P is shown in Fig. 5b. The peak intensity of Ge-P phonon mode is directly proportional to the concentration of isolated P atoms in the substitutional position. With increasing the P concentration the peak intensity increases and the peak position shifts towards higher wavenumber. Fukata et al. have attributed the Ge-P peak shift to the stress induced by

incorporation of high P concentration into the system [24]. In fact the, the covalent radius of P (107 pm) is about 11% smaller than that of Ge [38, 39]. This means that the heavily P doped Ge layer made by ion implantation should exhibit biaxial tensile strain. The biaxial tensile strain in group IV semiconductors causes the blue shift of the $TO_{Ge\text{-}Ge}$ phonon mode, which is also visible in Figure 5a. Therefore, in n-type Ge heavily doped with small covalent radius dopants like P the peak shift of the $TO_{Ge\text{-}Ge}$ phonon mode is caused by both the doping and biaxial tensile strain.

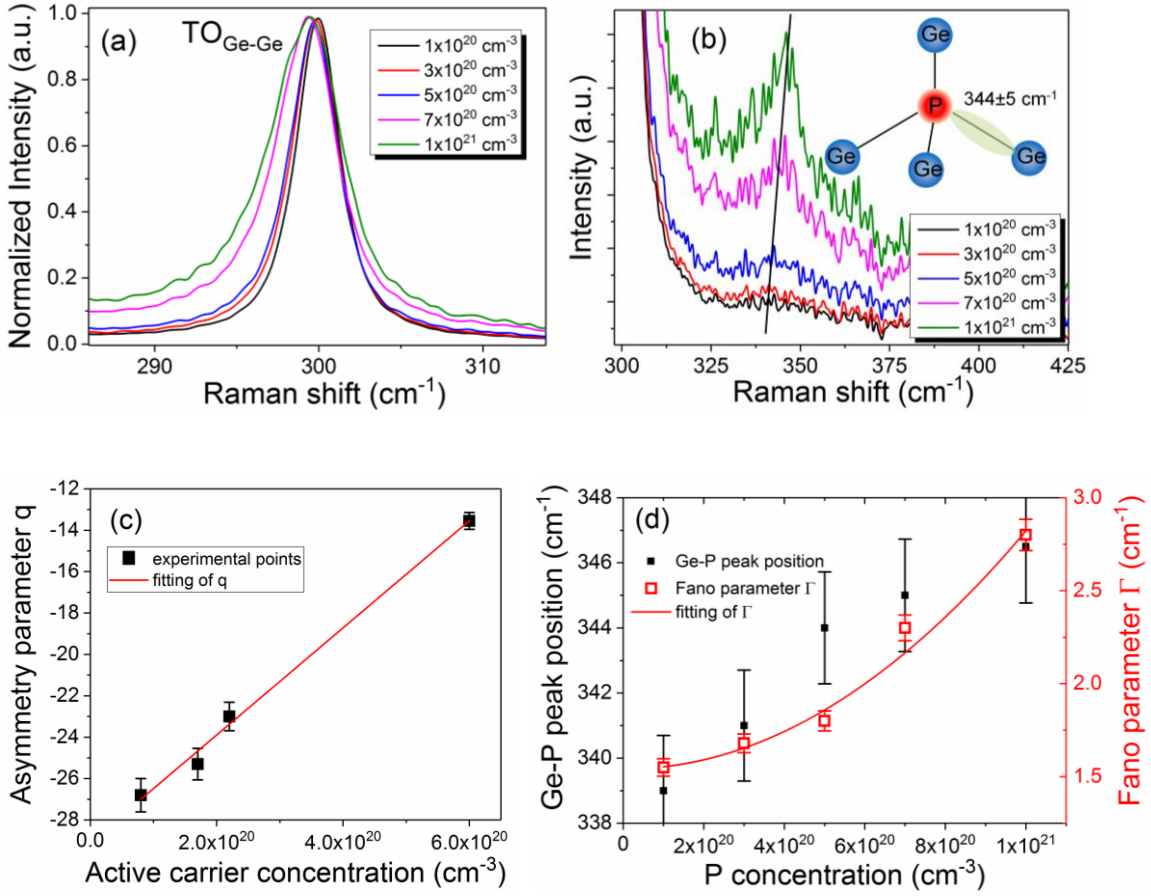

FIG. 5. (a) and (b) present the Raman spectra of the $TO_{Ge\text{-}Ge}$ phonon mode and the local vibrational phonon mode of Ge-P for different doping level, respectively. The dependence of the Fano asymmetry parameter q as a function of active carrier concentration (c) and the local vibrational peak intensity of the Ge-P Raman active phonon mode and the Fano parameter Γ obtained for the

main $TO_{Ge\text{-}Ge}$ phonon mode as a function of P concentration (d) in P-implanted Ge followed by FLA for 20 ms at an energy density of 95 Jcm^{-2}. The solid red line in (d) shows the parabolic fitting of the Fano parameter Γ.

The effective carrier concentration was estimated from Hall Effect measurements at 2.5 K which represents the concentration of electrically active P atoms at the substitutional position in the Ge lattice. The lowest electrically active P concentration that can be detected by our micro-Raman is in the range of 5×10^{19} cm^{-3} and the Ge-P phonon mode is located at 338.2 cm^{-1}. Due to the interaction of phonons with carriers the LO phonon mode in highly doped Ge becomes asymmetric. The asymmetry of the LO phonon mode in n-type Ge is due to the Fano interference which is given by:

$$I(\omega)=(q+\varepsilon)^2/(1+\varepsilon^2) + C \qquad (1)$$

and

$$\varepsilon=(\omega-\omega_0-\Delta\omega)/\Gamma \qquad (2)$$

where q is the asymmetry parameter, ω is the wavenumber, ω_0 is the position of the phonon mode in intrinsic and strain free Ge, Δω is the shift of the phonon mode due to the doping, C is the background coefficient and Γ is the line width parameter. The values of q and Γ are defined by the fraction of electrically active P atoms i.e. effective carrier concentration and the total P concentration, respectively.

The absolute value of asymmetry parameter q decreases with increasing the concentration of electrically active P (see Fig. 5 c). The dependence of q as a function of electron concentration n_e can be fitted with linear function:

$$q = a + b \times n_e \quad (3)$$

where a = -29.07 ±0.43 and b = 2.6×10^{-20} ±1×10^{-22}. For the sample with the effective carrier concentration of 8×10^{19} cm^{-3}, the q is found to be -26.55 and decreases down to -13.55 for n_e~ 6×10^{20} cm^{-3}. Recently, Boninelli et al. have used Raman spectroscopy to determine the carrier concentration in Ge doped by P implantation followed by laser melting [40]. They have shown that for n_e= 1×10^{20} cm^{-3} the asymmetry parameter q=-26.3. Using equation 3 and parameters a and b obtained by fitting the experimental results presented in Figure 4c the active carrier concentration in their sample for q=-26.3 is 1.05×10^{20} cm^{-3} which agrees perfectly with the value obtained by Hall effect and ECV [40]. Interestingly, the peak position of Ge-P local vibrational phonon modes also shifts with increasing P concentration, but the Ge-P phonon mode is expected to depend more on the total concentration of isolated P atoms in Ge than on the active carrier concentration. Figure 5d shows the change of the peak position of the Ge-P phonon mode (left axis) and the Fano parameter Γ (right axis) as a function of P concentration. Due to the fact that the carrier concentration increases with increasing P concentration, Γ exhibits the same tendency with increasing P concentration like with increasing the effective carrier concentration. Unfortunately, the two P atoms incorporated into the Ge lattice at the neighbouring position can form P-P dimers which forms deep donors and at room temperature they are not electrically active [14]. Moreover the P-P dimers cause the broadening of the Ge-P local vibrational mode. Hence, the n-type doping is a self-limiting process for very high P concentrations. However, the peak position of the Ge-P phonon mode saturates slowly when the P concentration approaches 1×10^{21} cm^{-1}. Taking into account the number of Ge atoms in 1 cm^{-3} and using strongly non-equilibrium processing the n-type doping of Ge beyond 10^{21} cm^{-3} should be possible. Unfortunately, the vacancy-donor complexes ($V\text{-}D_n$ with $n \leq 4$) are the main deactivation centers in n-type Ge. One vacancy can

deactivate up to four donors. Chroneos et al. have shown that $V\text{-}D_n$ complexes in Ge are thermodynamically stable at temperatures lower than 800 K [41, 42]. According to density functional theory calculations, at temperature higher than 850 K, the concentration of $V\text{-}D_4$ clusters progressively decreases liberating unbounded V and donor atoms [41, 42].

Recently, we have shown that ultra-doped n-type Ge with an electron concentration in the range of 10^{20} cm^{-3} or higher can be achieved by applying non-equilibrium methods, e.g. low-energy plasma-enhanced chemical vapour deposition or ion implantation followed by millisecond-range flash lamp annealing (FLA) [14, 26] where the maximum carrier concentration increases with decreasing the thickness of the doped layer. Most probably, it is due to the dissociation of $V\text{-}D_n$ complexes during millisecond range annealing. The released vacancies diffuse towards the surface and bulk Ge. Due to very short annealing time the diffusion of vacancies is limited. Therefore, the effective thickness of the ultra-doped Ge which can be liberated from vacancies during FLA is also limited. The change of the Fano parameter Γ as a function of P concentration in highly doped semiconductors can be described by $\Gamma=A+B*x + C*x^2$ where A, B and C are constants and x is the total P concentration. In contrast to Ref. 34, the Γ parameter does not saturate as a function of P concentration. The present technique (TERS and c-AFM) can be used to determine the concentration and distribution of carriers in any kind of nanostructures where the local vibrational phonon modes between the matrix atoms and dopant atoms are active Raman modes like: B and P in Si and Ge, or Si in GaAs.

Fig. 6 shows a typical dependence between the total resistance and the spacing between Ni stripes derived from TLM of samples after *in-situ* germanidation for 20 ms at an energy density of 95 Jcm^{-2}. The formation of ohmic contacts is confirmed by the linear behaviour of the current-voltage characteristics measured among neighbouring contacts (not shown). In order to extract the specific

contact resistance ρ_c, data points presented in Fig. 6 were linearly fitted to deduce the transfer length L_T and the contact resistance R_C. The sheet resistance (R_{Sh}) and ρ_c are respectively calculated by the following expressions: $R_{Sh} = \frac{R_C W}{L_T}$, and $\rho_C = R_{Sh} L_T^2$, where W is the length of the Ni-germanide stripes (viz. 200 μm). The resulting R_{sh} and ρ_c were found to be 0.74 Ω/sq and 8.7×10^{-6} Ωcm^2, respectively.

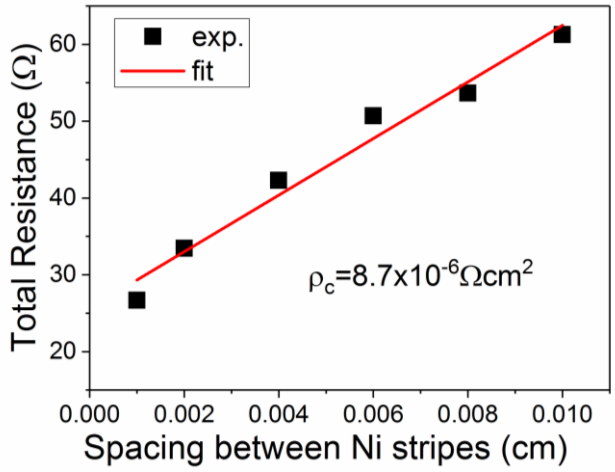

FIG. 6. The total resistance as a function of spacing between Ni stripes derived from TLM.

The carrier concentration estimated from the Hall effect data measured at 2.5 K obtained from the P implanted Ge after annealing at an energy density of 95 Jcm^{-2} is as high as $n_e=6\times10^{20}$ cm^{-3} while the electron mobility was found to be 29 cm^2/(V·s). The relatively low carrier mobility is thought to be caused by the Coulomb scattering. Taking into the account the doping level we should expect lower ρ_c. Most probably the contact quality between NiGe stripes and Ge plays a major role. The conventional method for the ohmic contact formation to n-type Ge relies on the germanidation process of Ni at about 400 ºC. The low temperature germanidation ensures the formation of single crystalline NiGe with sharp interface via solid phase epitaxy. In order to maximize the carrier concentration in P implanted Ge the germanidation process of Ni was performed at the annealing conditions optimized for the maximum activation of P. During our single-step process by FLA, the

Ni germanidation appears via liquid phase epitaxy.

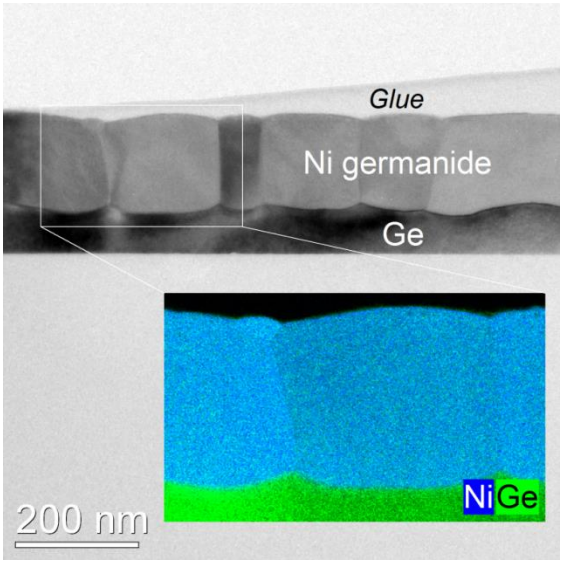

FIG. 7. Cross-sectional bright-field TEM image of a 50 nm thick Ni layer deposited onto GeOI after FLA for 20 ms together with superimposed Ni (blue) and Ge (green) element distributions based on EDXS obtained in scanning TEM mode for the region marked by the white rectangle.

In order to reduce the ρ_c and to keep high doping level the germanidation process can be carried out with two-step flash annealing when the second flash with low energy ensures the solid phase epitaxy of Ni-germanide. The Ni-germanidation using low energy flash and the influence of the multi-flash annealing on the activation/deactivation of donors in Ge will be investigated in the future. To characterize the microstructure after Ni germanidation, transmission electron microscope (TEM) analysis was performed. Fig. 7 shows a representative cross-sectional bright-field TEM image of the Ni-germanide layer formed on the top of Ge. Particular for the TEM investigation, the germanidation was performed using a 50 nm thick Ni layer. Even such thick Ni film is fully converted into Ni-germanide during a single 20 ms long flash pulse. The resulting ohmic contact is polycrystalline with an average grain size in the order of 200 nm. A well-defined interface between Ni-germanide and Ge is observed. The element composition of the fabricated

Ni-germanide was investigated by mapping the Ni and Ge element distributions (inset of Fig 7). Quantitative analysis reveals Ni concentrations between 53 and 57 at.-%.

4. Conclusions

We have utilized strongly non-equilibrium processing *i.e.* ion implantation followed by millisecond FLA to fabricate shallow n^{++}-p junction in GeOI. The maximum electron concentration in n-type Ge layers has been found to be 6×10^{20} cm^{-3}, *i.e.* 3-fold higher than the equilibrium solid solubility limit for P in Ge. The ohmic contacts formed to the n^{++} layer show specific contact resistance as low as 8.7×10^{-6} Ωcm^2. The germanidation of Ni was carried out *in-situ* and simultaneously with the P activation during a single 20 ms flash pulse, which avoids the unwanted deactivation of dopants in Ge as demonstrated by using conventional annealing methods such as rapid thermal annealing. Moreover, we have developed a simple methodology to probe and visualize the dopant distribution in heavily doped semiconductors using c-AFM and TERS. This approach can be easily implemented to investigate the electrical properties of any kind of semiconductors at nanoscale.

Conflicts of interest

There are no conflicts to declare.

Acknowledgement

Support by the Ion Beam Center (IBC) at HZDR is gratefully acknowledged. The authors would like to thank H. Hilliges, A. Kunz, and B. Scheumann from HZDR for their careful sample preparation. Funding of TEM Talos F200X by the German Federal Ministry of Education of

Research (BMBF), Grant No. 03SF0451 in the framework of HEMCP is gratefully acknowledged. Y. Berencén would like to thank the Alexander-von-Humboldt foundation for providing a postdoctoral fellowship.

References:

1. https://www.semiconductors.org/main/2015_international_technology_roadmap_for_semiconductors_itrs/
2. V. Deshpande, V. Djara, E. O'Connor, P. Hashemi, T. Morf, K. Balakrishnan, D. Caimi, M. Sousa, J. Fompeyrine and L. Czornomaz, *Jpn. J. Appl. Phys.* **56**, 04CA05 (2017).
3. T. E. Kazior, *Phil. Trans. R. Soc. A* **372**, 20130105 (2014).
4. J. Liu, L. C. Kimerling and J. Michel, *Semicond. Sci. Technol.* **27**, 094006 (2012).
5. R. Yu, *et al. Phys. Status Solidi RRL* **8**, 65–68 (2014).
6. P. Chaisakul, D. Marris-Morini, J. Frigerio, D. Chrastina, M-S. Rouifed, S. Cecchi, P. Crozat, G. Isella and L. Vivien, *Nat. Photon.* **8**, 4826 (2014).
7. S. Prucnal, *et al. Semicond. Sci. Technol.* **31**, 105012 (2016).
8. T. Sadoh, Y. Kai, R. Matsumura, K. Moto and M. Miyao, *Appl. Phys. Lett.* **109,** 232106 (2016).
9. J. Greil, A. Lugstein, C. Zeiner, G. Strasser and E. Bertagnolli, *Nano Lett.* **12**, 6230 (2012).
10. Y-C. Fang, K-Y. Chen, C-H. Hsieh, C-C. Su and Y-H. Wu, *ACS Appl. Mater. Interfaces* **7**, 26374−26380 (2015).
11. J. Kim, S. W. Bedell and D. K. Sadana, *Appl. Phys. Lett.* **101**, 112107 (2012).
12. G. Mattoni, W. M. Klesse, G. Capellini, M. Y. Simmons and G. Scappucci, *ACS Nano* **7**, 11310–11316 (2013).

13. S-H. Huang, F-L. Lu, W-L. Huang, C-H. Huang and C. W. Liu, *IEEE Electron Device Lett.,* **36**, 1114 (2015).

14. S. Prucnal, *et al., Sci. Rep*. **6***,* 27643 (2016).

15. H. Tanimura, *et al. MRS Advances* DOI: https://doi.org/10.1557/adv.2017.388.

16. S-S. Chuang, T-C. Cho, P-J. Sung, K-H. Kao, H. J. H. Chen, Y-J. Lee, M. I. Current and T-Y. Tseng, *ECS J. Solid State Sci. and Technol.* **6**, P350-P355 (2017).

17. X. Ou, P. Das Kanungo, R. Kögler, P. Werner, U. Gösele, W. Skorupa and X. Wang *Nano Lett.*, **10**, 171–175 (2010).

18. A. Vandooren, D. Leonelli, R. Rooyackers, A. Hikavyy, K. Devriendt, M. Demand, R. Loo, G. Groeseneken and C. Huyghebaert, *Solid-State Electronics* **83**, 50–55 (2013).

19. A. Schulze, A. S. Verhulst, A. Nazir, T. Hantschel, P. Eyben and W. A. Vandervorst, *J. Appl. Phys.* **113**, 114310 (2013).

20. B. Sermage, Z. Essa, N. Taleb, M. Quillec, J. Aubin, J. M. Hartmann and M. Veillerot, *J. Appl. Phys.* **119**, 155703 (2016).

21. G. Contreras, A. Compaan and A. Axmann, *J. Phys. Colloques* **44**, (C5), C5-193-C5-195 (1983).

22. N. Fukata, *Phys. Status Solidi C* **11**, 320–330 (2014).

23. N. Fukata, *Adv. Mater.* **21**, 2829–2832 (2009).

24. N. Fukata, M. Yu, W. Jevasuwan, T. Takei, Y. Bando, W. Wu and Z. L. Wang, *ACS Nano* **9**, 12182–12188 (2015).

25. K. Gallacher, P. Velha, D. J. Paul, I. MacLaren, M. Myronov and D. R. Leadley, *Appl. Phys. Lett.* **100**, 022113 (2012).

26. S. Prucnal *et al. Semicond. Sci. Technol.* **32**, 115006 (2017).

27. S. Prucnal, L. Rebohle and W. Skorupa, *Mater. Sci. Semicond. Process,* **62**, 115-127 (2017).

28. R. Milazzo *et al. Appl. Phys. Lett.* **110**, 011905 (2017).

29. J. F. Ziegler, *Nucl. Instr. Meth. B* **219-220**, 1027 (2004).

30. P. Śpiewak, J. Vanhellemont, K. Sueoka, K. J. Kurzydłowski,and I. Romandic, *J. Appl. Phys.* 103, 086103 (2008).

31. R. D. Rodriguez, E. Sheremet, S. Müller, O. D. Gordan, A. Villabona, S. Schulze, M. Hietschold and D. R. T. Zahn, *Rev. Sci. Instrum.* **83**, 123708 (2012).

32. S. B. M. Castro, S. Barnola and B. Glück, *Journal of Integrated Circuits and Systems* **8**, 104-109 (2013).

33. Y. H. Lee and M-M. Chen, *J. Vac. Sci. Technol. B* **4**, 468 (1986).

34. P. S. Goley and M. K. Hudait, *Materials* **7**, 2301-2339 (2014).

35. N. Fukata, K. Sato, M. Mitome, Y. Bando, T. Sekiguchi, M. Kirkham, J-I. Hong, Z. L. Wang and R. L. Snyder, *ACS Nano* **4**, 3807–3816 (2010).

36. U. Fano, *Phys. Rev.* **124**, 1866–1878 (1961).

37. N. Fukata, M. Mitome, T. Sekiguchi, Y. Bando, M. Kirkham, J. Hong, Z. L. Wang and R. L. Snyder, *ACS Nano* **6**, 8887–8895 (2012).

38. S. Prucnal et al. *Phys. Rev. Appl.* **10**, 064055 (2018).

39. C. Xu, C. L. Senaratne, J. Kouvetakis, and J. Menendez, *Phys. Rev. B* **93**¸041201 (2016).

40. A. Boninelli, R. Milazzo, R. Carles, F. Houdellier, R. Duffy, K. Huet, A. La Magna, E. Napolitani, and F. Cristiano, APL Materials **6**, 058504 (2018).

41. A. Chroneos, and H. Bracht, Appl. Phys. Rev. 1, 011301 (2014).

42. A. Chroneos, Mater. Sci. Semicond. Process. 15, 691–696 (2012).